



Published in final edited form as:

*Med Image Anal.* 2016 April ; 29: 12–23. doi:10.1016/j.media.2015.11.004.

## Shape Analysis of Hypertrophic and Hypertensive Heart Disease using MRI-based 3D Surface Models of Left Ventricular Geometry

Siamak Ardekanj<sup>a,b</sup>, Saurabh Jain<sup>a</sup>, Alianna Sanzi<sup>a</sup>, Celia P. Corona-Villalobos<sup>c</sup>, Theodore P. Abraham<sup>c</sup>, M. Roselle Abraham<sup>c</sup>, Stefan L. Zimmerman<sup>c</sup>, Katherine C. Wu<sup>c</sup>, Raimond L. Winslow<sup>b</sup>, Michael I. Miller<sup>a,b</sup>, and Laurent Younes<sup>a,b</sup>

<sup>a</sup>Center for Imaging Science, Johns Hopkins University, USA

<sup>b</sup>Institute for Computational Medicine, Johns Hopkins University, USA

<sup>c</sup>Johns Hopkins University Medical Institutions, USA

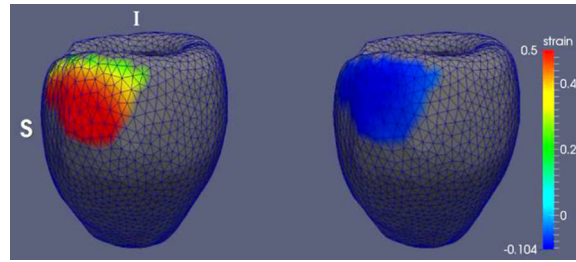
### Abstract

The focus of this study was to develop advanced mathematical tools to construct high-resolution 3D models of left-ventricular (LV) geometry to evaluate focal geometric differences between patients with hypertrophic cardiomyopathy (HCM) and hypertensive heart disease (HHD) using cardiac magnetic resonance (MR) cross-sectional images. A limiting factor in 3D analysis of cardiac MR cross-sections is the low out-of-plane resolution of the acquired images. To overcome this problem, we have developed a mathematical framework to construct a population-based high-resolution 3D LV triangulated surface (template) in which an iterative matching algorithm maps a surface mesh of a normal heart to a set of cross-sectional contours that were extracted from short-axis cine cardiac MR images of patients who were diagnosed with either HCM or HHD. A statistical analysis was conducted on deformations that were estimated at each surface node to identify shape differences at end-diastole (ED), end-systole (ES), and motion-related shape variation from ED to ES. Some significant shape difference in radial thickness was detected at ES. Differences of LV 3D surface geometry were identified focally on the basal anterior septum wall. Further research is needed to relate these findings to the HCM morphological substrate and to design a classifier to discriminate among different etiologies of LV hypertrophy.

### Graphical abstract

---

**Publisher's Disclaimer:** This is a PDF file of an unedited manuscript that has been accepted for publication. As a service to our customers we are providing this early version of the manuscript. The manuscript will undergo copyediting, typesetting, and review of the resulting proof before it is published in its final citable form. Please note that during the production process errors may be discovered which could affect the content, and all legal disclaimers that apply to the journal pertain.



## Keywords

surface-to-contour mapping; 3D left-ventricular geometry; cardiac MRI; Cardiomyopathy

## 1. Introduction

Left-ventricular hypertrophy (LVH) is a nonspecific thickening of the myocardium that develops in response to a variety of physiologic or pathologic stimuli (Weidemann et al., 2010). Among the pathologic stimuli, hypertension is the most common cause of LVH (Gardin, 2004), and results from a compensatory response to pressure overload of the left ventricle and an increase in systolic wall stress (Weidemann et al., 2010). Among other pathologic causes, hypertrophic cardiomyopathy (HCM) is the most common genetic cardiomyopathy and is caused by sarcomere mutations (Weidemann et al., 2010). HCM exhibits significant heterogeneity in the disease course and clinical presentation, and is considered to be the leading cause of sudden cardiac death in competitive athletes and young individuals in the United States (Maron, 2003). Identifying the etiology of hypertrophy is clinically relevant as it would determine the treatment strategy. Currently, only 50–60% of patients with HCM phenotype have a sarcomere protein mutation (Wheeler et al., 2009) prompting the need for other measures to identify these patients. The clinical diagnosis of HCM has been based on the demonstration of an otherwise unexplained increase in left ventricular (LV) wall thickness in the presence of a non-dilated LV cavity (Nagueh et al., 2011; Gersh et al., 2011). While the LV maximal wall thickness is, in general, more pronounced in HCM patients compared to that seen in hypertensive patients (HHD), prior studies have identified considerable overlap in these two populations (Petersen et al., 2005) with respect to the simple ventricular geometry indices, including maximal end-diastolic wall thickness. Therefore, differentiating solely based on these measures is considered challenging.

Cardiac magnetic resonance (MR) imaging can generate intrinsically three-dimensional (3D) images that can be used to obtain regional ventricular shape and function in any plane without ionizing radiation. However, despite the 3D nature of cardiac MR, most of the LVH-related studies have relied on in-plane information (Noureldin et al., 2012; Puntmann et al., 2010; Sipola et al., 2011). This stems from the fact that the out-of-plane resolution of MR images is low and a 3D reconstruction of the geometry requires interpolation (Frangi et al., 2002) or surface-fitting to endocardial and epicardial contours using some predefined geometry (Wang et al., 2009). Either of these approaches could potentially introduce an unnecessary geometric constraint, and consequently mask subtle geometric differences

between different etiologies of LVH. Recently, we have developed a new mathematical tool to non-rigidly match a high-resolution surface mesh constructed from a multi-detector CT image of the heart to a set of LV epicardial and endocardial contours that were extracted from cardiac MR (Ardekani et al., 2012). The matching algorithm estimates the optimum solution by identifying the closest point on the triangulated mesh to the contour points on the LV curves. In certain cases, when there are large shape variations between the surface mesh and LV cross-sections, for example due to pathology, the matching algorithm may fail by attracting mesh surface to the wrong contour (e.g. epicardial surface to the endocardial contour and vice versa). In this work, we present an extension to our prior work that resolves this problem and allows optimum surface-to-curve mapping in situations where one has to account for large shape differences (such as those due to pathology or a difference in cardiac phase). Using this mathematical tool, we are able to perform a detailed statistical analysis of LV 3D geometry using only sparse sets of 2D plane contours as observations, without relying on parametric geometric models such as those based on prolate spheroidal coordinates (Nielsen et al., 1991), therefore facilitating cross-subject examination of shape variation between different populations. An essential step for population-based shape analysis is the construction of an average geometry that can be mapped to the shape of individual subjects. By mapping a common reference geometry to the LV cross-sections from different subjects that are collected at different locations across the LV, one can leverage important prior information to characterize the 3D geometry variation within the population, which goes a long way beyond direct interpolation between cross-sections. We applied this mathematical framework to characterize regional shape- and motion-related differences between HCM and HHD populations based on the speculation that due to differences in the underlying mechanisms that govern LVH in HCM and HHD populations, there would be subtle differences in the remodeling pattern that can be potentially identified using shape analysis performed at a high spatial resolution.

## 2. Theory

In this section, we describe our approach to map a triangulated mesh to a set of sparse contours that constitute the LV geometry (Section 2.1). Next using this matching approach, we outline the construction of an average LV mesh in Section 2.2. The average LV mesh which we refer to as the template is used to perform cross-population shape variation analysis as explained in Section 3.9.

### 2.1. Surface-to-curve Mapping

The non-linear surface-to-curve matching method that was used here is an extension of our prior work (Ardekani et al., 2012). This algorithm uses the large deformation diffeomorphic metric mapping (LDDMM) method (Beg et al., 2005) to identify an optimum deformation that maps the triangulated surface mesh to the LV cross-sections. For each point on the LV contours, the algorithm minimizes the distance between that point and the point closest to it on the deformed template surface, while ensuring a smooth deformation field and wall compatibility (preventing points in the epicardial (resp. endocardial) surface from being mapped to points in the opposite contour on the LV cross-sections). This process can be

described in more detail using the following mathematical framework, in which one optimizes the sum of a deformation cost and a data cost penalty.

**2.1.1. Deformation Cost**—Let  $S^{(0)}$  be an initial surface. The deformation cost in LDDMM involves a time-dependent surface  $S(t)$ ,  $t \in [0, 1]$  that we represent as a mapping  $x \mapsto S(t, x)$  from  $S^{(0)}$  to  $\mathbb{R}^3$ , with  $S(0, x) = x$ . It is defined as

$$F(S(\cdot)) = \min \left\{ \int_0^1 \|v(t)\|_V^2 : v \in V, v(t, S(t, x)) = \partial_t S(t, x) \right\}$$

where  $V$  is a reproducing kernel Hilbert space of vector fields with kernel  $(x, y) \mapsto K(x, y)$ , where  $K(x, y)$  is a 3 by 3 matrix. (In our experiments, we use a Gaussian kernel,  $K(x, y) = g(\|x - y\|) \text{Id}_{\mathbb{R}^3}$  with  $g(t) = \exp(-t^2/2d^2)$  for some parameter  $d$ ).

We now take the special case of discrete triangulated surfaces, in which  $S^{(0)} = (x^{(0)}, T^{(0)})$  where  $x^{(0)}$  is a set of  $n$  distinct vertices, and  $T^{(0)}$  is a set of faces (triples of vertex indexes) that describe the surface topology. Letting  $S(t) = (x(t), T^{(0)})$  be the evolving surface, one can prove that the optimal velocity,  $v$ , can be parametrized as

$$v(t, x) = \sum_{l=1}^n K(x, x_l) \alpha_l(t)$$

where  $\alpha_1, \dots, \alpha_n$  are unknown time-dependent 3D vectors. The optimization problem is then reduced to the form:

$$\text{minimize } F(S(\cdot)) = \int_0^1 F(x(t), \alpha(t)) dt,$$

$$\text{where } F(x, \alpha) = \sum_{k,l=1}^n \alpha_k^T K(x_k, x_l) \alpha_l,$$

$$\text{subject to } \partial_t x_k = \sum_{l=1}^n K(x_k, x_l) \alpha_l$$

Using a matrix notation, we identify  $\alpha$  and  $x$  with  $3n$ -dimensional vectors, and define  $G_x$  as the matrix formed with the 3 by 3 blocks  $K(x_k, x_l)$ , so that  $x = G_x \alpha$  and  $F(x, \alpha) = \alpha^T G_x \alpha$ .

**2.1.2. Data Cost**—The observation in our experiments is a collection of oriented curves  $\Gamma = \{\gamma_1, \dots, \gamma_k\}$ , all supported in a cross-sectional plane. Since our method applies to more general contexts, we will assume here that each curve  $\gamma \in \Gamma$  is supported by a plane  $P_\gamma$ , which may depend on  $\gamma$ . Our goal is to deform the initial surface  $S^{(0)}$  to align it with the

curves in  $\Gamma$ , ensuring that the orientations are consistent. We let  $Z_\gamma$  denote a unit normal vector to this plane.

We now define a cost function  $S \mapsto U(S, \Gamma)$ , which measures the proximity of a surface  $S$  to this collection, in such a way that  $U$  is always positive and vanishes if and only if every  $\gamma \in \Gamma$  is supported on  $S$  with a consistent orientation. We express  $U$  as a sum of two terms,  $U = U_0 + U_c$ , each of which is described below. We let  $y_1, \dots, y_n$  denote the vertices in  $S$  (note that  $y_k = x_k(1)$  with the notation of the previous paragraph).

Let  $N_S$  denote the normal to  $S$ , and let  $v_\gamma$  denote the normal to  $\gamma$  in the plane  $P_\gamma$ , where  $\gamma \in \Gamma$ . Both these normals are defined according to the orientations of  $S$  and  $\gamma$  respectively. We say that  $N_S$  and  $v_\gamma$  are consistent with each other if the projection of  $N_S$  on  $P_\gamma$  is collinear to  $v_\gamma$  and points in the same direction as  $v_\gamma$  (Fig. 1). In other words,  $N_S = \lambda v_\gamma + \mu Z_\gamma$ , for some  $\lambda$  and  $\mu$ , where  $\lambda \geq 0$  and  $Z_\gamma$  denotes the normal to  $P_\gamma$ . Such a property is true if  $\gamma$  is inscribed in  $S$  and oriented consistently. Accordingly, we define  $U_0$  via integrals along curves, as follows:

$$U_0(S, \Gamma) = \frac{1}{\sigma^2} \sum_{\gamma \in \Gamma} \int_{y \in S} \inf g(y, N_S(y), \gamma(s), v_\gamma(s), Z_\gamma) ds \quad (1)$$

where  $s$  is the arc length in each integral and  $g(y, N, x, v, Z)$  is a positive function that is minimized when (1)  $y = x$  and (2)  $N = \lambda v + \mu Z$  with  $\lambda \geq 0$ . One can take, for example

$$g(y, N, x, v, Z) = \frac{1 + |x - y|^2 / \tau^2}{\sqrt{a^2 + \max(N^T v, 0)^2 + (N^T Z)^2}} - \frac{1}{\sqrt{a^2 + 1}}$$

In this case, the numerator in the first fraction is always larger than 1, with equality if and only if  $x = y$ ; since  $1 = \|N_S\|^2 = (N^T (Z \times v))^2 + (N^T v)^2 + (N^T Z)^2$ , the denominator is always smaller than  $\sqrt{a^2 + 1}$  with equality if  $N$  belongs to the plane generated by  $v$  and  $Z$ , with  $N^T v \geq 0$ . Thus  $g$  satisfies the required conditions. The parameter  $\tau$  is a scale factor for the distance between points on the curves and the surface, and  $a$  is a small positive constant that prevents division by 0.

The second part of the data cost term,  $U_c$  imposes soft constraints on the deformed surface. When a plane shows no intersection with the endocardium, one can infer a linear inequality ensuring that the deformed surface only lies on one side of this plane, which takes the form  $Z^T y \leq c$  or  $Z^T y \geq c$  where  $Z$  is the normal to this plane (the direction of the inequality is easily inferred from the position of other planes that do intersect with the endocardium). Moreover, for short-axis planes, finding only one curve in the intersection indicates that the plane lies near the apex, “below” the interior wall of the apex and “above” the exterior wall of the apex. This results in an inequality constraint restricted to the points in the interior wall. The second part of the cost function reflects these constraints using soft penalties. To define the soft penalty, let  $H$  be a smooth approximation to the function  $x \mapsto \kappa \max(x, 0)$ , namely,

$$H(x) = \kappa \log(e^{x/\kappa} + 1) \quad (2)$$

Then assuming, without loss of generality, that we have a series of constraints taking the form  $y_q^T Z_j \leq c_j$  for  $q \in A_j \subset \{1, \dots, n\}$ , and for  $j = 1, \dots, m$ , we take

$$U_c(S, \Gamma) = \sum_{j=1}^m \sum_{q \in A_j} H(y_q^T Z_j - c_j).$$

The penalty terms defined above require normals to be defined on the vertices of a triangulated surface  $S = (x, T)$ . We define the vertex normals as follows: Let  $f = (i, j, k) \in T$  be a face. Let

$$N_S(f) = \frac{1}{2} (x_j - x_i) \times (x_k - x_i) \quad (3)$$

be the area-weighted normal to the face. Then, for a vertex  $x_u$ :

$$N_S(x_u) \propto \sum_{f: u \in f} N_S(f) \quad (4)$$

(normalized to have unit norm).

**2.1.3. Objective function**—Now assume that a sequence  $\Gamma(1), \dots, \Gamma(m)$  is observed for each subject. Each  $\Gamma(i)$  is a set of curves corresponding to sparse cross-sections of one of the LV geometries obtained from the cine MR images of a given subject at some time in its cardiac cycle (e.g., ED and ES). Associate to them a sequence of times  $0 < t_1 < \dots < t_m$ . Given an initial surface  $S^{(0)} = (x^{(0)}, T^{(0)})$ , we minimize

$$E(\alpha) = \int_0^{t_m} F(x(t), \alpha(t)) dt + \sum_{i=1}^m U(S(t_i), \Gamma(i))$$

subject to the constraints  $x(0) = x^{(0)}$ ,  $S(t) = (x(t), T^{(0)})$  and  $\dot{x}(t) = G_{x(t)} \alpha(t)$ . This cost function is minimized by alternating the following two steps:

- i. Fix  $\alpha$  and  $x$ . For each  $i = 1, \dots, m$  and each  $\gamma \in \Gamma(i)$ , determine an index  $k_\gamma(s)$  such that

$$g(\gamma(s), \nu_\gamma(s), x_{k_\gamma(s)}(t_i), N_{S(t_i)}(x_{k_\gamma(s)}(t_i)), Z_\gamma) = \inf_{y \in S(t_i)} g(\gamma(s), \nu_\gamma(s), y, N_{S(t_i)}(y), Z_\gamma)$$

- ii. Let

$$U^*(x(t_i), \Gamma(i)) = \frac{1}{\sigma^2} \sum_{\gamma \in \Gamma(i)} \int_{\gamma} g(\gamma(s), \nu_\gamma(s), x_{k_\gamma(s)}(t_i), N_{S(t_i)}(x_{k_\gamma(s)}(t_i))),$$

with  $N_{S(t)}$  given by (4). Update  $\alpha$  and  $x$  by running a few gradient descent steps to minimize

$$E^*(x, \alpha) = \int_0^{t_m} F(x(t), \alpha(t)) dt + \sum_{i=1}^m U^*(x(t_i), \Gamma(i)) \quad (5)$$

with  $x(0) = x^{(0)}$  and  ${}_t x(t) = G_{x(t)} \alpha(t)$ .

The overall cost function is minimized using the adjoint method in optimal control, as described, for example, in (Vaillant and Glaunes, 2005; Glaunès et al., 2006; Cotter and Holm, 2009; Azencott et al., 2010; Younes, 2012), and summarized in the appendix. This method is applied in this paper either with  $m = 1$  and  $t_1 = 1$ , with  $\Gamma^{(1)}$  segmented either from ED or ES phases and  $S^{(0)}$  being accordingly an ED or ES template (computed as described in the next section), or with  $m = 2$ ,  $t_1 = 1$ ,  $t_2 = 2$ , with  $\Gamma^{(1)}$  corresponding to ED,  $\Gamma^{(2)}$  to ES, and  $S^{(0)}$  being an ED template. For surface-to-curve matching results presented in this paper, the following parameters were used: the kernel width  $d$  associated with the function  $F$  was 30. The penalty weight for the term  $U_c$  was 1.5 and the value of  $\kappa$  in function  $H$  in equation 2 was 1, the value of  $\tau$  in function  $g$  was 1, the weight for the deformation cost was 0.5, and the number of descent steps for optimization was 200.

## 2.2. Template Estimation

Equipped with our surface-to-curve matching algorithm, we are able to construct an average geometry from the set of LV contours extracted from the subjects in the population. This average geometry is used to evaluate shape variability. It is desirable for such an average shape to be built based on the statistical properties of the population being study, thereby minimizing potential distortions that may arise from large mismatches between the template shape and individual geometries. We start with an initial LV geometry and estimate a reference LV shape assuming that the LV geometries in the population are generated by randomly deforming the reference shape. To proceed with the mathematical presentation of our approach, we use the notation introduced in the previous paragraph, and assume that a population with  $M$  subjects is available. To simplify the discussion, we further assume that only one time point is used per subject, and denote the associated population of the sets of curves by  $\Gamma^{(1)}, \dots, \Gamma^{(M)}$ .

We assume that a surface  $\mathcal{S}^{(h)}(x^{(h)}, T^{(h)})$  is given, which we call the hypertemplate. Our goal is to estimate a template surface,  $\mathcal{S}^{(T)} = (x^{(T)}, T^{(h)})$ , as a deformation of  $\mathcal{S}^{(h)}$ , such that  $\mathcal{S}^{(T)}$  provides a high-resolution shape average of the LV cross-sections that constitute the dataset. The template is estimated by minimizing

$$E(X, A) = \lambda \int_0^1 F_0(x^{(0)}(t), \alpha^{(0)}(t)) dt + \sum_{k=1}^M \int_0^1 F_k(x^{(k)}(t), \alpha^{(k)}(t)) dt + \sum_{k=1}^M U(S^{(k)}(1), \Gamma^{(k)}) \quad (6)$$

where  $X = (x^{(0)}, \dots, x^{(M)})$ ,  $A = (\alpha^{(0)}, \dots, \alpha^{(M)})$ ,  $\mathcal{S}^{(k)}(t) = (x^{(k)}(t), T^{(h)})$ , with constraints

$$\begin{cases} x^{(0)}(0) = x^{(h)} \\ x^{(k)}(0) = x^{(0)}(1), \quad k=1, \dots, M \\ \partial_t x^{(k)} = G_{x^{(k)}(t)} \alpha^{(k)}(t), \quad k=0, \dots, M. \end{cases}$$

The quantity of interest, here, is the template set of vertices  $x^{(T)} := x^{(0)}(1)$ , which acts as a hub from which the trajectories that connect to observed data originate. The minimization follows the same principle as the one described for the time series problem, alternating the determination of optimal “anchors” that achieved the inf in the definition of  $U$ , and the minimization of (6) with  $U$  replaced by  $U^*$ , in which the inf is evaluated at the anchors. As before, this second step uses the adjoint algorithm, which is described in the appendix.

It is also possible to use a different kernel for the deformation of the hypertemplate (with the associated function  $F_0$ ) without changing much of the computation. In this study, for both ED and ES template estimations, the kernel width  $d$  associated with the functions  $F_0$  and  $F_k$  were set to 25. The penalty weight for the term  $U_c$  was 1.5 and the value of  $\kappa$  in function  $H$  in equation 2 was 1 for both ED and ES template estimations. The values of  $\tau$  in function  $g$  were 1 and 0.1 for the ED and ES template estimations, respectively. The values of  $\lambda$  were 1 and 0.0001 for the ED and ES template estimations, respectively. The number of descent steps for the optimization algorithm was 200.

### 3. Methods

#### 3.1. Subjects

All human studies were approved by the Johns Hopkins Institutional Review Board for human investigation. All patients were enrolled in a single-center prospective study of either hypertensive heart disease or hypertrophic cardiomyopathy. For the current study, 20 patients (11 with HHD and 9 with familial HCM) were studied. Table 1 summarizes the demographic information along with the scalar volumetric and mass measurements of the LV for these two populations. The inclusion criteria for the HHD patients were: a positive history of hypertension and an echocardiogram showing LV hypertrophy (maximum wall thickness  $>12$  mm) and/or diastolic dysfunction and LV ejection fraction greater than 45%, with or without symptomatic heart failure (New York Heart Association functional class I-III). For the HCM patients, they were: asymmetric septal hypertrophy exceeding 15 mm, septal to posterior wall thickness ratio  $<1.5$ , in the absence of hypertension and other conditions known to cause ventricular hypertrophy such as valvular heart disease; with or without systolic anterior motion of the mitral valve and/or left ventricular outflow obstruction. Patients with prior coronary revascularization or history of myocardial infarction were excluded, as were patients with abnormal renal function. The pattern of ventricular hypertrophy for the subjects in the HCM population is listed in Table 2.

#### 3.2. Image Acquisition

Magnetic resonance imaging was performed using a 1.5 T Siemens Avanto (Erlangen, Germany) scanner with cardiac-phased-array receiver coil. Steady-state free precession (SSFP) cine images were acquired for nine to fourteen contiguous short-axis slices to cover

the entire LV. SSFP cine 4 and 2 chamber long-axes views were also obtained. LV volumes, mass, and LV ejection fraction (LVEF) were obtained by manual contouring of the endocardial surface in end-diastole and end-systole using dedicated software (MASS, Medis, Leiden, The Netherlands). Sequence parameters were: repetition time (TR) 2.2–2.6 ms, echo time (TE) 1.1–1.3 ms, in-plane resolution 1.0–1.5×1.0–1.5 mm, flip angle  $\alpha=65\text{--}80^\circ$ , 8-mm slice thickness, 0–2 mm gap, and temporal resolution 40–50 ms.

### 3.3. Shape Analysis

We conducted our shape analysis in two steps: First, we performed the shape analysis of the LV geometry at two distinct time points (ED and ES) separately. Then, we examined contraction-related shape differences from ED to ES between HCM and HHD populations (McEachen et al.). Both analyses rely on the construction of a 3D hypertemplate surface, represented as a dense triangulated surface. This hypertemplate was then deformed into “shape averages” (or population templates) computed separately for the ED and ES phases (see Section 2.2). The populations were then registered to the relevant shape average, resulting in a shape representation in a common coordinate system, which was then used as an input to the statistical analysis. This work flow is summarized in Fig. 2, and we now proceed to a detailed description of each step.

### 3.4. Preprocessing

The hypertemplate was built from a computed tomography- (CT) based axial image of a normal subject that was acquired at ED. For this image, the myocardium was segmented by manual outlining of epicardial and endocardial surfaces (papillary muscles and trabeculations were excluded). A triangulated surface mesh of the masked CT left ventricle with 2851 nodes and 5698 faces was constructed and the surface mesh was resampled to construct uniform triangulations (Valette et al., 2008).

For the MRI data, epicardial and endocardial contours were isolated using *Segment* (Heiberg et al., 2010), a semi-automatic freely available software (Fig. 2a). Each segmentation was quality-controlled by a trained radiologist with extensive experience in cardiovascular MRI. Slice-to-slice misalignments of the short axis (SAX) contours that occur due to the cardiac MRI acquisition at separate breath-holds were corrected (Fig. 2b) using a method that was previously described in (Ardekani et al., 2012), in which horizontal and vertical long-axis epicardial and endocardial contours at ED and ES are used to identify optimum in-plane translation of SAX contours in order to restore the slice-to-slice alignment. It has been shown that in-plane translation as a first order approximation can be used to remedy 3D rotation and translation problems due to breath-hold misregistration (McLeish et al., 2002).

Three-dimensional rigid mappings between the cross-sectional contours and the high-resolution surface templates (Figs. 2d and 2f) were conducted in two steps. In step 1, two landmarks were used to identify the closest point to the apex and the mid-chamber point at the mitral valve location to roughly estimate the long axis of LV cross-sections in the SAX contours and the high-resolution surface mesh. Then, the long axis of LV curves of individual subjects and of the surface mesh of the reference geometry were aligned with the z-axis. This places contours in the short axis plane (scanner coordinate) into a horizontal

plane that is roughly parallel to the  $xy$ -plane. Finally, using two mid-ventricular insertion points (placed where the right ventricle connects to the left ventricle free wall at the middle of LV chamber) for each subject's LV contours and for the surface template, we apply the method described in (Horn, 1987), to estimate a single optimum transformation that rotates all contour points around the  $z$  axis and translates them into the coordinate system of the surface mesh nodes (template).

### 3.5. Matching Shape Averages to LV Cross-sections

Our shape analysis method relies on constructing two average LV shapes (Section 2.2), one for ED and one for ES (Fig. 2c). In this approach we align the LV geometry of different subjects against a common reference shape. Note that this computation used every subject (HCM and HHD together), either at ES or ED, which makes it group independent. Once the average high-resolution LV surfaces were constructed, regional shape variations among different subjects could be studied by performing a linear matching, followed by a non-linear matching of the average shape to the individual LV contours (Fig. 2d). Displacements of mesh nodes computed from the non-linear matching represent how much deformation is required to match the average template to the individual subject's LV contours, and how these deformations vary from one subject to another. These deformations were used to derive shape metrics (Section 3.9) on which statistical analyses were performed (Fig. 2e).

### 3.6. ED-to-ES Shape Mappings

For each subject, we rigidly registered the ED contours onto the ED template surface and applied the same rigid transformation to the ES contours of that subject (Figs. 2f and 2g). Since both ED and ES phases are represented by cross-sections, and in order to continue using triangulated mesh representations, we used the method that is described in Section 2.1.3 to map a global ED template to the ED contours and then to the ES contours of each subject (Fig. 2h). This enabled us to directly transport transformation vector fields from the ED-to-ES mesh to the topologically equivalent shape average mesh for statistical analysis (Fig. 2i).

### 3.7. Validation of Surface-to-curve Matching

To evaluate the accuracy of our surface-to-curve matching algorithm, we constructed high-resolution triangulated surface meshes from LV CT images of 5 different subjects (reconstructed image resolution of  $0.29\text{--}0.31 \times 0.29\text{--}0.31 \times 0.75 \text{ mm}^3$ ) that were acquired at ED. One of these surfaces was randomly selected and used as the template surface. All the surfaces were reoriented in a way that their long axis aligned with the  $z$  axis of the coordinate system. From the 4 remaining surfaces, we generated cross-sections that were 10 mm apart (the same as the out of plane resolution plus the slice gap in our MRI study), and were perpendicular to the LV long axis. These resulted in a set of contours similar to what we observe from the cardiac MRI short axis images. Following the same procedure that is described in Section 3.4, these contours were rigidly matched to the template surface mesh. The same rigid transformation was also applied to the corresponding triangulated surface mesh from which the contours were extracted. Then, we matched the template surface mesh to each of the contour sets using the surface-to-curve matching algorithm. For comparison, we also matched the template surfaced mesh to the corresponding surface mesh. The

matching error was calculated via estimating the shortest distance between the deformed template mesh nodes on the epicardial and endocardial surfaces to the corresponding epicardial and endocardial curve points, respectively. This procedure was repeated for surface-to-surface matching.

### 3.8. Template Estimation Consistency

To evaluate the consistency of the template estimation algorithm with respect to the choice of the hypertemplate, we used 5 different surface meshes that were constructed from high-resolution CT data. These 5 hypertemplates were first placed in a common coordinate system and then used to generate final templates from the population data as described in Section 2.2. We then evaluated the similarity between the estimated templates using the average closest point distance error. This error identifies the distance between a particular surface mesh node in one template to the closest surface mesh node on another, and was calculated for epicardial and endocardial surfaces separately.

### 3.9. Statistical Analysis

The transformation vector fields that define the shape deformation to the LV contours of an individual subject were used to identify shape differences between the two populations. Following global alignment (rotation and translation), we examined the regional shape differences between the two populations by computing two different quantitative metrics: 1) the log of the ratio of the surface area of triangulated faces in the shape template before and after the deformation and 2) the Lagrangian strain tensor. The surface area ratio (SAR) defines how much surface area expansion or shrinkage is required to map a template LV geometry to a particular subject's LV geometry. The strain tensors were computed using  $E \propto (D\varphi^T D\varphi - I)$ , where  $\varphi$  is the transformation vector field that maps the template mesh to individual target contours,  $D$  is the differential operator, and  $I$  is the identity matrix. The strain tensor ( $E$ ) describes the local deformation in the squared norm. It is symmetric and can be projected onto a particular direction to examine the magnitude of the change in length along that direction. In this framework, negative strain values are interpreted as local shortening of the myocardium of the subject relative to the template, and positive values as local elongation. To facilitate the physiologic interpretation of the results, we defined a local coordinate system for each surface mesh node representing three perpendicular orientations: radial, circumferential, and longitudinal. The strain tensor that was calculated at each node was projected onto these directions to produce radial, circumferential and longitudinal strain values. These values subsequently were used to perform a shape analysis of the LV geometry at ED and ES, and to study the motion-related shape alteration from ED to ES. Note that since we are not following some fiducial points for mapping (as opposed to tagged MRI), the strain tensor that is estimated here will not represent motion components that are not observable from changes in geometry, such as torsion. In other words, it reflects shape variation, but not necessarily a genuine motion. Henceforth, to differentiate the estimated strain values in our experiments from the ones that are generated using tagged MRI, we will use the term *geometric strain*.

We performed the statistical analysis of these geometric strain values and SAR at two levels. First, we examined the whole LV geometry for any group differences. If we were able to

identify statistically significant group differences then we analyzed groups at the mesh node level to isolate regions along the myocardial surface contributing to the group difference. Our statistical analysis is based on a randomized Analysis of Covariance (ANCOVA) test using permutation of residuals (Anderson and Braak, 2003). This approach allows us to determine if there are any differences in the shape parameters between two population cohorts while controlling for the effect of the LV mass index (see the limitations section). The details are as follows: (i) For each surface node  $k$  in subject  $S$ , we define a statistical general model which is given by:  $J_k(s) = \beta_{k,0} + \beta_{k,1} Y(s) + \alpha_{cov} X_{cov}(s) + \varepsilon_k(s)$ , where  $Y(s)$  is a group variable that determines if subject  $S$  belongs to either the HCM or the HHD group.  $X_{cov}(s)$  is a common covariate for subject  $S$  (in this study we used the LVM normalized by subject's height to the power of 2.7 as a covariate) and  $\varepsilon_k$  is an error term. The null hypothesis at node  $k$  assumed that  $\beta_{k,1}$  equals zero. (ii) Next, at each node  $k$ , we

computed the  $F$  statistic as  $F_k = \frac{RSS_0}{RSS} - 1$ , where  $RSS_0$  is the residual sum of squares under the null hypothesis and  $RSS$  is the residual sum of squares under the general model. (iii) Then, a permutation test with 40,000 permutations was used to estimate a p-value corrected for multiple comparisons. To do so, at each permutation, we collected the maximum statistic ( $F^* = \max_k(F_k)$ ). This gave the permutation distribution of the maximum statistic. The estimated p-value for the whole surface is the proportion of the permutation distribution for  $F^*$  that is greater or equal to the statistic computed for the actual subject labeling at the surface level. Letting  $f^*$  be the 0.95 quantile statistic of the permutation distribution, we estimate a set of nodes on which the null hypothesis is rejected at the 5% family-wise error rate (FWER) to be  $\{k : F_k \geq f^*\}$ . The FWER approach ensures that the probability of making one or more false discoveries remain below the alpha level (here 0.05) while performing multiple hypothesis testing (one test per node).

## 4. Results

Fig. 3 illustrates the performance of the distance matching algorithm using LDDMM. It is clear that in situations where there are large shape differences between the template surface and the cross-sectional contours (e.g. matching a normal to a diseased heart or matching different cardiac phases), a conventional distance matching algorithm would fail. However, by incorporating consistent orientation constraints into the data cost term, we ensured an accurate mapping of the surface mesh onto the target contours. Figs. 4 and 5 provide the mean and standard deviation of the LDDMM surface-to-curve matching against LDDMM surface-to-surface matching. The overall distance error at the level of cross-sections is less than 1.5 mm and is comparable to what we observe in surface-to-surface matching indicating high accuracy of our surface-to-curve matching. However, we also notice that at locations where there are no cross-sections such as the apex or the base of the heart, the average distance error can reach up to 4 or 5 mm.

The results of template estimation consistency are listed in Table 3. Careful examination of this table indicates a good resemblance among 5 different templates constructed using the template estimation algorithm. In particular, hypertemplate No. 4 is largely different from other templates as demonstrated by the closest point distance error. After template estimation using hypertemplate No. 4, the distance error between the estimated template and

the other templates is significantly reduced, and is consistent with the other estimated templates.

The statistical analysis of the LV geometry at ES indicated a significant difference between the two populations with respect to the radial geometric strain (corrected  $p \approx 0.00025$ ). In addition to the radial geometric strain, the circumferential geometric strain was also significant (corrected  $p \approx 0.017$ ), however, the longitudinal geometric strain was not significant (corrected  $p \approx 0.05$ ). The statistical analysis of the LV geometry at ED between the two populations was not significant for any of geometric strain values (radial: corrected  $p \approx 0.18$ , circumferential: corrected  $p \approx 0.32$ , longitudinal: corrected  $p \approx 0.13$ ). The motion-related shape analysis of the LV geometry from ED to ES was only statistically significant (although weakly) for the radial geometric strain (radial: corrected  $p \approx 0.045$ , circumferential: corrected  $p \approx 0.12$ , longitudinal: corrected  $p \approx 0.54$ ). We did not detect any statistically significant difference between the two populations with respect to the SAR values.

To identify the nature of regional differences between the two populations, we constructed mean geometric strain value surface maps (estimated from the regression model) for each population group to represent the difference in a particular geometric strain value between the HCM and the HHD populations. These maps define the nature of shape variation placed on a common coordinate system. A careful examination of the radial geometric strain (Fig. 6) maps placed over the statistically significant region at ES indicates that the basilar septal and the anterior epicardial walls in the HCM patients are significantly thicker along this direction. We also detected a statistically significant difference between HCM and HHD populations with respect to the circumferential geometric strain at ES. However, this difference was limited to very few mesh nodes (not shown).

## 5. Discussion

In this work, we have presented an advanced shape modeling approach to identify detailed 3D regional shape differences between two important and common etiologies of LV hypertrophy using sparse cross sections of the LV that were extracted from cardiac MRI. We identified regional shape differences at ES and motion-related geometry differences from ED to ES, suggesting that the pattern of cardiac remodeling is governed by the underlying etiology. Identifying regional differences in remodeling requires tools that allow for a characterization of regional shape and function variation of the left ventricle after remodeling. Cross-sectional-based imaging modalities such as cardiac MRI or 3D ultrasound could potentially provides 3D information about the LV geometry. However, in practice, only global volume-derived indices such as EF and/or the in-plane geometry information are used to describe the shape differences among patients with HCM. Volumetric indices only measure the global cardiac function, which lacks detailed spatial information, and in-plane geometry metrics are prone to wall thickness measurement inconsistency due to acquisition-related differences in imaging plane to wall angles (Tobon-Gomez et al., 2010; Beyar et al., 1990). The proposed method overcomes these problems by constructing high-resolution surface maps of ventricles using contours extracted from image cross-sections.

Using our computational tool, we examined both static (ED and ES) and dynamic (ED-to-ES) shape variations between HCM and HHD populations. Differentiating HCM from HHD based on wall thickness is a challenging clinical task. They both present with different degrees of myocardial wall thickening (Maron, 2012). Wall thickening associated with HCM is asymmetric and in some cases non-contiguous (Maron, 2012). Therefore, the radial geometric strain can be used to evaluate differences in regional radial thickness between these two groups. Moreover, it is likely that differences in the pattern of hypertrophy causes different responses in myocardial shape and contraction as measured by regional longitudinal shortening, circumferential narrowing, and radial thickening. The surface area ratio is another metric that can be used to determine if asymmetric pattern of hypertrophy in HCM patients is associated with asymmetric pattern of surface expansion or shrinkage. Regional shape differences between the two populations at ED were not significant, which can be attributed to the fact that the selection criterion for the hypertrophic cardiomyopathy relies on the measure of wall thickness in ED (Noureldin et al., 2012). However, we identified significantly larger regional shape differences between the two populations at ES, which may indicate that measuring shape differences at ES enhances the discriminating power. The basal anterior septum with the contiguous anterior free wall is a common place for myocardial hypertrophy seen in HCM subjects (Maron, 2012). Our results at ES indicate that patients with HCM, on average, have larger radial geometric strain in this region relative to HHD patients. This shows that relative to the reference shape, larger displacements along the surface radial direction (larger radial thickness) is required to map the template geometry to the HCM patients' LV geometry. Interestingly larger radial thickness was only observed along the epicardial surface in HCM subjects relative to HHD patients, highlighting the non-uniform pattern of remodeling in HCM both over the LV surface and within the myocardium.

The shape alteration of the LV from ED-to-ES was only weakly significant along the radial direction. It is likely that differences in the global scale that could exist due to the heterogeneity within the populations has contributed to our shape analysis result. Normal gender- and age-related variation in the cardiac size and function has been reported previously (Lin et al., 2008). Identifying and quantifying these normal variations will be crucial to distinguish disease states from normal conditions. The fact that body size accounts for up to 50% of adult LV dimensions variability (Pelliccia et al., 1999) indicates that scaling of parameters that are derived from the global LV shape could potentially reduces normal physiologic variations. The nature of this scaling has been under debate and it has been proposed that scaling should be consistent with the geometry (Dewey et al., 2008). We should also recognize that these variations could arise from both normal physiological and pathological sources. Despite this ambiguity, the observed shape differences between these two populations using the ES cardiac phase (without incorporating the global scale) provides additional encouraging evidence that analyzing the cardiac shape at ES could potentially distinguish between different etiologies of LVH.

There have been few prior studies using cardiac MRI to evaluate anatomical LV geometry differences between HCM and HHD patients (Petersen et al., 2005; Sipola et al., 2011; Wagner et al., 1991). These studies used both geometric indices derived from MR cross-sections and volume parameters to distinguish between several causes of LVH (athlete's

heart, HCM, and HHD). While these parameters were able to differentiate between physiological (athlete's heart) and pathological (HCM and HHD) causes of LVH, they were less successful in identifying the cause of pathological hypertrophy. Previously, computational shape algorithms were applied on the CT images of left ventricles to characterize shape differences between ischemic and non-ischemic cardiomyopathy (Ardekani et al., 2009). More recently, finite element mesh models of the LV extracted from cardiac MRI combined with principal component analysis have been proposed to identify components of global shape variation in the adult asymptomatic population (Medrano-Gracia et al., 2014) or to quantify remodeling in patients with myocardial infarction corrected for acquisition bias (Zhang et al., 2014; Medrano-Gracia et al., 2013). The proposed method here provides an alternative approach to evaluate the LV geometry at the surface mesh node level as opposed to the global or segmental levels, thereby providing an avenue to characterize sub-segmental differences in remodeling, and in the evolution of the myocardial response in the HCM and HHD population cohorts.

### 5.1 Study Limitations

One limitation of the current study is the modest number of subjects. However, the fact that significant differences in ventricular shape between the two groups were detected using conservative non-parametric statistical tests is an encouraging indication for using our approach with larger datasets. Another potential limitation is that in the current study, the HCM population consisted of an almost equal number of male and female patients, compared to mainly male subjects in the HHD population. Using animal and human models, it has been shown that women have an increased hypertrophic response to pressure overload (Carroll et al., 1992; Rohde et al., 1997; Weinberg et al., 1999). Therefore it would be important to account for gender-related differences in the LV when studying shape variation. Prior studies have indicated that using the LV mass index (LV mass normalized by height<sup>2.7</sup>) as a covariate, as was done in our study, could reduce the impact of gender-related LVH differences (de Simone et al., 1992; Foppa et al., 2005). In our implementation of LDDMM surface-to-curve matching, we only used information from the short-axis images. This choice was based on the availability of clinical data. When available, additional information such as long axis images can be included in the algorithm to improve the accuracy of shape matching in the apical and basal regions. Finally, in this study we only explored ED-to-ES shape variation since these two time points represent functional phases that can be easily identified in all subjects. However, our algorithm by design can be extended to several time points.

## 6. Conclusion

Advanced mathematical models can be used to extract and identify detailed 3D spatial information regarding the differences in patients with LV hypertrophy due to HCM and HHD. These models can be potentially useful in discriminating HCM and HHD in complex cases where HCM patients have concomitant hypertension, therefore assisting physicians in designing appropriate therapeutic strategies.

## Acknowledgment

This research was supported by several grants from the National Institute of Health (R24HL085343, HL109968, HL103812, HL098046).

## Appendix A. Adjoint method for Time Series

We describe here how to compute the gradient of  $E^*$  described in equation (5), given by

$$E^*(x, \alpha) = \int_0^{t_m} \alpha(t)^T G_{x(t)} \alpha(t) dt + \sum_{i=1}^m U^*(x(t_i), \Gamma(i))$$

in which  $x$  is considered as a function of  $\alpha$  via the constraint  $x(0) = x^{(0)}$ ,  $\dot{x}(t) = G_{x(t)} \alpha(t)$ .

Introduce a so-called *covector*  $t \mapsto p(t)$  and the *Lagrangian*

$$L(x, \alpha, p) = E^*(x, \alpha) + \int_0^{t_m} p(t)^T (\partial_t x - G_{x(t)} \alpha(t)) dt.$$

Assuming variations  $\delta x$  and  $\delta \alpha$ , we can write

$$\begin{aligned} \delta L = & 2 \int_0^{t_m} \alpha(t)^T G_{x(t)} \delta \alpha(t) dt + \int_0^{t_m} \nabla_x (\alpha(t)^T G_{x(t)} \alpha(t))^T \delta x(t) dt \\ & + \int_0^{t_m} p(t)^T \alpha_t \delta x(t) dt - \int_0^{t_m} \delta \alpha(t)^T G_{x(t)} p(t) dt \\ & - \int_0^{t_m} \nabla_x (p(t)^T G_{x(t)} \alpha(t))^T \delta x(t) dt \\ & + \frac{1}{\sigma^2} \sum_{i=1}^m \nabla_x U^*(x(t_i), \Gamma(i))^T \delta x(t_i) \end{aligned}$$

Note that  $\delta x(0) = 0$  since  $x(0)$  is fixed. Choosing  $p$  such that

1.  $\dot{p} = -\nabla_x ((p(t) - \alpha(t))^T G_{x(t)} \alpha(t))$
2.  $p(t_m) = -\nabla_x U^*(x(t_m), \Gamma(m))$
3.  $p(t_j^-) = p(t_j^+) - \nabla_x U^*(x(t_j), \Gamma(j))$ , for  $j = 1, \dots, m-1$

Then, writing

$$\int_0^{t_m} p(t)^T \partial_t \delta x(t) dt = p(t_m) \delta x(t_m) + \sum_{j=1}^{m-1} (p(t_j^-) - p(t_j^+)) \delta x(t_j) - \int_0^{t_m} \partial_t p(t)^T \delta x(t) dt,$$

the variation reduces to

$$\delta L = \int_0^{t_m} (2\alpha(t) - p(t))^T G_{x(t)} \delta \alpha(t) dt$$

This gives the differential  $\alpha E^*(t) = (2\alpha(t) - p(t))^T G_{x(t)}$ . One can use the gradient conditioned by the positive definite matrix  $G_x$  in the minimization algorithm, which has the simple expression  $\nabla^G E^* = 2\alpha - p$ . The gradient (or conjugate gradient) descent algorithm to minimize  $E$  is then designed as follows:

1. Given current value of  $\alpha$ , compute the time evolutions of  $x$ .
2. Compute the gradients of each of the attachment terms  $U^*$  at  $x(t_j)$  for  $j = 1, \dots, m$ . Recall that the normal vector that appears in  $U^*$  is defined from finite differences via (3) and (4). The computation of its gradient is detailed in Appendix C.
3. Solve equations in conditions 1 to 3 above (backward in time) to compute the covector  $p$ .
4. Update the current estimate of  $\alpha$  using the gradient obtained from the updated covectors.
5. Repeat 1 – 4 until convergence.

## Appendix B. Adjoint Method for Template Estimation

The gradient of  $E$  (or rather,  $E^*$ ) with respect to  $A$  in equation (6) is computed in a similar way. One now introduces  $M+1$  covectors  $p^{(0)}, p^{(1)}, \dots, p^{(M)}$  and the Lagrangian

$$L(X, A, p) = E(X, A) + \sum_{k=0}^M \int_0^1 p^{(k)}(t)^T (\partial_t x^{(k)}(t) - G_{x^{(k)}(t)} \alpha^{(k)}(t)) dt$$

Expressing a variation  $\delta L$  as a function of  $\delta X$  and  $\delta A$ , one specifies the time evolution and boundary conditions of the covector in order to cancel the terms involving  $\delta x$ , making possible the identification of the differential in  $\alpha$ . skipping the details, one finds that, with

1.  $p^{(k)}(1) = -x U^*(x^{(k)}(1), \Gamma^{(k)})$  for  $k = 1, \dots, M$ ,
2.  $p^{(k)} = -\nabla_x ((p^{(k)}(t) - \alpha^{(k)}(t))^T G_{x^{(k)}(t)} \alpha^{(k)}(t))$ , for  $k = 1, \dots, M$ ,
3.  $p_0(1) = \sum_{k=1}^M p_k(0)$
4.  $p^{(0)} = -\nabla_x ((p^{(k)}(t) - \lambda \alpha^{(0)}(t))^T G_{x^{(0)}(t)} \alpha^{(0)}(t))$ , for  $k = 1, \dots, M$ ,

the variation reduces to

$$\delta L = \int_0^1 (2\lambda \alpha^{(0)}(t) - p^{(0)}(t))^T G_{x^{(0)}(t)} \delta \alpha^{(0)}(t) dt + \sum_{k=1}^M \int_0^1 (2\alpha^{(k)}(t) - p^{(k)}(t))^T G_{x^{(k)}(t)} \delta \alpha^{(k)}(t) dt \quad (\text{B.1})$$

This gives the (conditionned) gradient

$$\begin{cases} \nabla_{\alpha^{(k)}}^G E^* = 2\alpha^{(k)} - p^{(k)} \text{ for } k=1, \dots, M \\ \nabla_{\alpha^{(0)}}^G E^* = 2\lambda \alpha^{(0)}(t) - p^{(0)}(t) \end{cases} \quad (\text{B.2})$$

## Appendix C. Gradient of the Data Cost Term

Let  $S = (x, T)$  be a triangulated surface, with  $x = (x_1, \dots, x_n)$  and  $\gamma$  a curve in a horizontal plane, discretized into a finite number of points,  $p_1, \dots, p_r$  with associated length elements

$\ell_1, \dots, \ell_r$  so that an integral of a function  $f$  over  $\gamma$  is approximated by  $\sum_{i=1}^r f(p_i)\ell_i$ .

Associate to each  $p_i$  an index  $k_i \in \{1, \dots, n\}$  and let

$$U^*(x, \gamma) = \sum_{i=1}^r g(p_i, \nu_i, x_{k_i}, N_{k_i}(x), Z_\gamma)\ell_i$$

where  $\nu_i$  is the horizontal unit normal to  $\gamma$  at  $p_i$  and  $N_{k_i}(x)$  the unit normal to  $S$  at  $x_{k_i}$  computed according to (3) and (4). We want to compute the derivative of  $U^*$  with respect to  $x$ .

If  $f$  is a face in  $T$  and  $k \in F$ , we denote by  $u_k^f$  the edge opposed to  $x_k$  in the triangle representing  $f$  in  $S$  (oriented according to the face orientation: if  $f = (k, i, j)$ , then  $u_k^f = x_j - x_i$  and it is easy to see that

$$\partial_{x_k} N(f)\delta x_k = \frac{1}{2} u_k(f) \times \delta x_k$$

if  $k \in f$  and 0 otherwise. Letting  $a_j(x) = |\sum_{f:j \in f} N(f)|$  so that

$$N_j(x) = \frac{1}{a_j(x)} \sum_{f:j \in f} N(f),$$

we find that

$$\partial_{x_k} N_j(x)\delta x_k = \frac{1}{2a_j(x)} \left( \sum_{f:j,k \in f} (u_k(f) \times \delta x_k - N_j(x)^T (u_k(f) \times \delta x_k) N_j(x)) \right).$$

Now

$$\begin{aligned} \partial_{x_k} U^*(x, \gamma)\delta x_k &= \sum_{i:k_i=k} \ell_i (\nabla_x g(p_i, \nu_i, x_k, N_k)^T \delta x_k + \nabla_N g(p_i, \nu_i, x_k, N_k)^T \partial_{x_k} N_k(x)\delta x_k) \\ &+ \sum_{j,j \sim k} \sum_{i:k_i=j} \ell_i \nabla_N g(p_i, \nu_i, x_j, N_j)^T \partial_{x_k} N_j(x)\delta x_k \end{aligned}$$

where  $j \sim k$  indicates that  $j$  and  $k$  are neighbors in  $T$ . Now, for any vector  $\mu$ , we can write

$$\begin{aligned}\mu^T \partial_{x_k} N_j(x) \delta x_k &= \frac{1}{2a_j(x)} \left( \sum_{f:j,k \in f} (\mu^T u_k(f) \times \delta x_k - N_j(x)^T (u_k(f) \times \delta x_k) \mu^T N_j(x)) \right) \\ &= \frac{1}{2a_j(x)} \left( \sum_{f:j,k \in f} (\mu - \mu^T N_j(x) N_j(x)) u_k(f) \right)^T \delta x_k.\end{aligned}$$

This implies that, denoting, for short,  $\nabla_x g_{ik} = \nabla_x g(p_i, v_i, x_k, N_k)$  and  $\nabla_N g_{ik} = \nabla_N g(p_i, v_i, x_k, N_k)$ ,

$$\begin{aligned}\nabla_{x_k} U^*(x, \gamma) &= \sum_{i:k_i=k} \ell_i \nabla_x g_{ik} \\ &+ \sum_{i:k_i=k} \frac{\ell_i}{2a_k(x)} \sum_{f:k \in f} (\nabla_N g_{ik} - \nabla_N g_{ik}^T N_k(x) N_k(x)) \times u_k(f) \\ &+ \sum_{j:j \sim k: k_i=j} \sum_{i:k_i=j} \frac{\ell_i}{2a_j(x)} \sum_{f:j,k \in f} (\nabla_N g_{ij} - \nabla_N g_{ij}^T N_j(x) N_j(x)) \times u_k(f)\end{aligned}$$

It then remains to plug-in the expressions

$$\nabla_x g_{ik} = \frac{2(x_k - p_i)}{(\tau^2 \sqrt{a^2 + \max(N_k^T \nu_i, 0)}^2 + (N_k^T Z_\gamma)^2)}$$

and

$$\nabla_N g_{ik} = - \frac{1 + |p_i - x_k|^2 / \tau^2}{(a^2 + \max(N_k^T \nu_i, 0)^2 + (N_k^T Z_\gamma)^2)^{3/2}} (\max(N_k^T \nu_i, 0) \nu_i + Z_\gamma)$$

to obtain the explicit expression of  $\nabla_{x_k} U^*(x, \gamma)$ . We can then write

$$\partial_{x_k} U^*(x, \Gamma) = \sum_{\gamma \in \Gamma} \nabla_{x_k} U^*(x, \gamma) + \kappa \sum_{j=1}^n (H^T(x_k^T Z_j - c_j) \delta_{x_k \in A_j}) Z_j.$$

## References

- Anderson M, Braak CT. Permutation tests for multi-factorial analysis of variance. *Journal of Statistical Computation and Simulation*. 2003; 73:85–113. URL: <http://dx.doi.org/10.1080/00949650215733>.
- Ardekani, S.; Jain, A.; Jain, S.; Abraham, T.; Abraham, M.; Zimmerman, S.; Winslow, R.; Miller, M.; Younes, L. Matching sparse sets of cardiac image cross-sections using large deformation diffeomorphic metric mapping algorithm. In: Camara, O.; Konukoglu, E.; Pop, M.; Rhode, K.; Sermesant, M.; Young, A., editors. *Statistical Atlases and Computational Models of the Heart. Imaging and Modelling Challenges*. Springer Berlin / Heidelberg: volume 7085 of *Lecture Notes in Computer Science*; 2012. p. 234-243. URL: <http://www.springerlink.com/content/g5576u4n25325176/abstract/>.

- Ardekani S, Weiss RG, Lardo AC, George RT, Lima JAC, Wu KC, Miller MI, Winslow RL, Younes L. Computational Method for Identifying and Quantifying Shape Features of Human Left Ventricular Remodeling. *Annals of Biomedical Engineering*. 2009; 37:1043–1054. URL: <http://link.springer.com/article/10.1007/s10439-009-9677-2>. [PubMed: 19322659]
- Azencott R, Glowinski R, He J, Jajoo A, Li Y, Martynenko A, Hoppe R, Benzekry S, Little S, Zoghbi W. Diffeomorphic matching and dynamic deformable surfaces in 3d medical imaging. *Computational Methods in Applied Mathematics*. 2010; 10:235–274.
- Beg MF, Miller MI, Troun A, Younes L. Computing Large Deformation Metric Mappings via Geodesic Flows of Diffeomorphisms. *International Journal of Computer Vision*. 2005; 61:139–157.
- Beyar R, Shapiro EP, Graves WL, Rogers WJ, Guier WH, Carey GA, Soulen RL, Zerhouni EA, Weisfeldt ML, Weiss JL. Quantification and validation of left ventricular wall thickening by a three-dimensional volume element magnetic resonance imaging approach. *Circulation*. 1990; 81:297–307. URL: <http://circ.ahajournals.org/content/81/1/297>. [PubMed: 2297833]
- Carroll JD, Carroll EP, Feldman T, Ward DM, Lang RM, McGaughey D, Karp RB. Sex-associated differences in left ventricular function in aortic stenosis of the elderly. *Circulation*. 1992; 86:1099–1107. URL: <http://circ.ahajournals.org/content/86/4/1099>. [PubMed: 1394918]
- Cotter C, Holm D. Continuous and discrete clebsch variational principles. *Foundations of Computational Mathematics*. 2009; 9:221–242.
- Dewey FE, Rosenthal D, Murphy DJ, Froelicher VF, Ashley EA. Does size matter? clinical applications of scaling cardiac size and function for body size. *Circulation*. 2008; 117:2279–2287. URL: <http://circ.ahajournals.org/content/117/17/2279>. [PubMed: 18443249]
- Foppa M, Duncan BB, Rohde LE. Echocardiography-based left ventricular mass estimation. how should we define hypertrophy? *Cardiovascular Ultrasound*. 2005; 3:17. URL: <http://www.cardiovascularultrasound.com/content/3/1/17/abstract>. [PubMed: 15963236]
- Frangi A, Rueckert D, Schnabel J, Niessen W. Automatic construction of multiple-object three-dimensional statistical shape models: application to cardiac modeling. *Medical Imaging, IEEE Transactions on*. 2002; 21:1151–1166.
- Gardin JM. Left ventricular hypertrophy: The next treatable, silent killer? *JAMA: The Journal of the American Medical Association*. 2004; 292:2396–2398. URL: <http://jama.jamanetwork.com/article.aspx?articleid=199789>.
- Gersh BJ, Maron BJ, Bonow RO, Dearani JA, Fifer MA, Link MS, Naidu SS, Nishimura RA, Ommen SR, Rakowski H, Seidman CE, Towbin JA, Udelson JE, Yancy CW. 2011 ACCF/AHA guideline for the diagnosis and treatment of hypertrophic cardiomyopathy: A report of the american college of cardiology Foundation/American heart association task force on practice guidelines developed in collaboration with the american association for thoracic surgery, american society of echocardiography, american society of nuclear cardiology, heart failure society of america, heart rhythm society, society for cardiovascular angiography and interventions, and society of thoracic surgeons. *Journal of the American College of Cardiology*. 2011; 58:e212–e260. URL: <http://www.sciencedirect.com/science/article/pii/S0735109711022753>. [PubMed: 22075469]
- Glaunés J, Trouné A, Younes L. Modeling planar shape variation via hamiltonian flows of curves. *Statistics and Analysis of Shapes*. 2006:335–361.
- Heiberg E, Sjgren J, Ugander M, Carlsson M, Engblom H, Arheden H. Design and validation of segment–freely available software for cardiovascular image analysis. *BMC medical imaging*. 2010; 10:1. URL: <http://www.ncbi.nlm.nih.gov/pubmed/20064248>, PMID: 20064248. [PubMed: 20064248]
- Horn BKP. Closed-form solution of absolute orientation using unit quaternions. *Journal of the Optical Society of America A*. 1987; 4:629. URL: <https://www.osapublishing.org/josaa/abstract.cfm?uri=josaa-4-4-629>.
- Lin FY, Devereux RB, Roman MJ, Meng J, Jow VM, Jacobs A, Weinsaft JW, Shaw LJ, Berman DS, Callister TQ, Min JK. Cardiac chamber volumes, function, and mass as determined by 64-multidetector row computed tomography: Mean values among healthy adults free of hypertension and obesity. *JACC: Cardiovascular Imaging*. 2008; 1:782–786. URL: <http://www.sciencedirect.com/science/article/pii/S1936878X08003690>. [PubMed: 19356515]

- Maron BJ. Sudden death in young athletes. *The New England journal of medicine*. 2003; 349:1064–1075. URL: <http://www.ncbi.nlm.nih.gov/pubmed/12968091>, PMID: 12968091. [PubMed: 12968091]
- Maron MS. Clinical Utility of Cardiovascular Magnetic Resonance in Hypertrophic Cardiomyopathy. *Journal of Cardiovascular Magnetic Resonance*. 2012; 14:13. URL: <http://www.jcmr-online.com/content/14/1/13/abstract>. [PubMed: 22296938]
- McEachen J, Nehorai A, Duncan J. Temporal estimation of cardiac non-rigid motion in image sequences. *Proceedings of the 40th Midwest Symposium on Circuits and Systems*. 1997; 2:901–904.
- McLeish K, Hill D, Atkinson D, Blackall J, Razavi R. A study of the motion and deformation of the heart due to respiration. *IEEE Transactions on Medical Imaging*. 2002; 21:1142–1150. [PubMed: 12564882]
- Medrano-Gracia P, Cowan BR, Ambale-Venkatesh B, Bluemke DA, Eng J, Finn JP, Fonseca CG, Lima JA, Suinesiaputra A, Young AA. Left ventricular shape variation in asymptomatic populations: the multi-ethnic study of atherosclerosis. *Journal of Cardiovascular Magnetic Resonance*. 2014; 16:56. URL: <http://jcmr-online.com/content/16/1/56/abstract>. [PubMed: 25160814]
- Medrano-Gracia P, Cowan BR, Bluemke DA, Finn JP, Kadish AH, Lee DC, Lima JA, Suinesiaputra A, Young AA. Atlas-based analysis of cardiac shape and function: correction of regional shape bias due to imaging protocol for population studies. *Journal of Cardiovascular Magnetic Resonance*. 2013; 15:80. URL: <http://www.jcmr-online.com/content/15/1/80/abstract>. [PubMed: 24033990]
- Nagueh SF, Bierig SM, Budoff MJ, Desai M, Dilsizian V, Eidem B, Goldstein SA, Hung J, Maron MS, Ommen SR, Woo A. American society of echocardiography clinical recommendations for multimodality cardiovascular imaging of patients with hypertrophic cardiomyopathy: Endorsed by the american society of nuclear cardiology, society for cardiovascular magnetic resonance, and society of cardiovascular computed tomography. *Journal of the American Society of Echocardiography*. 2011; 24:473–498. URL: <http://www.sciencedirect.com/science/article/pii/S0894731711001891>. [PubMed: 21514501]
- Nielsen PM, Le Grice IJ, Smaill BH, Hunter PJ. Mathematical model of geometry and fibrous structure of the heart. *The American Journal of Physiology*. 1991; 260:H1365–H1378. [PubMed: 2012234]
- Noureldin RA, Liu S, Nacif MS, Judge DP, Halushka MK, Abraham TP, Ho C, Bluemke DA. The diagnosis of hypertrophic cardiomyopathy by cardiovascular magnetic resonance. *Journal of Cardiovascular Magnetic Resonance*. 2012; 14:17. URL: <http://www.jcmr-online.com/content/14/1/17/abstract>. [PubMed: 22348519]
- Pelliccia A, Culasso F, Di Paolo FM, Maron BJ. Physiologic left ventricular cavity dilatation in elite athletes. *Annals of Internal Medicine*. 1999; 130:23–31. URL: <http://dx.doi.org/>. [PubMed: 9890846]
- Petersen SE, Selvanayagam JB, Francis JM, Myerson SG, Wiesmann F, Robson MD, Ostman-Smith I, Casadei B, Watkins H, Neubauer S. Differentiation of athlete’s heart from pathological forms of cardiac hypertrophy by means of geometric indices derived from cardiovascular magnetic resonance. *Journal of cardiovascular magnetic resonance: official journal of the Society for Cardiovascular Magnetic Resonance*. 2005; 7:551–558. URL: <http://www.ncbi.nlm.nih.gov/pubmed/15959967>. PMID: 15959967. [PubMed: 15959967]
- Puntmann VO, Jahnke C, Gebker R, Schnackenburg B, Fox KF, Fleck E, Paetsch I. Usefulness of magnetic resonance imaging to distinguish hypertensive and hypertrophic cardiomyopathy. *The American Journal of Cardiology*. 2010; 106:1016–1022. URL: [http://www.ajconline.org/article/S0002-9149\(10\)01169-0/abstract](http://www.ajconline.org/article/S0002-9149(10)01169-0/abstract). [PubMed: 20854967]
- Rohde M, Zhi M, Aranki M, Beckel M, Lee M, Reimold M. Gender-associated differences in left ventricular geometry in patients with aortic valve disease and effect of distinct overload subsets. *The American Journal of Cardiology*. 1997; 80:475–480. URL: <http://www.sciencedirect.com/science/article/pii/S0002914997003986>. [PubMed: 9285661]
- de Simone G, Daniels SR, Devereux RB, Meyer RA, Roman MJ, de Divitiis O, Alderman MH. Left ventricular mass and body size in normotensive children and adults: Assessment of allometric relations and impact of overweight. *Journal of the American College of Cardiology*. 1992;

20:1251–1260. URL: <http://www.sciencedirect.com/science/article/pii/S073510979290385Z>. [PubMed: 1401629]

- Sipola P, Magga J, Husso M, Jskelinen P, Peuhkurinen K, Kuusisto J. Cardiac MRI assessed left ventricular hypertrophy in differentiating hypertensive heart disease from hypertrophic cardiomyopathy attributable to a sarcomeric gene mutation. *European Radiology*. 2011; 21:1383–1389. URL: <http://www.springerlink.com/content/0534r733494t1432/abstract/>. [PubMed: 21274714]
- Tobon-Gomez, C.; Butakoff, C.; Yushkevich, P.; Huguët, M.; Frangi, A. 3D mesh based wall thickness measurement: Identification of left ventricular hypertrophy phenotypes; *Engineering in Medicine and Biology Society (EMBC), 2010 Annual International Conference of the IEEE*; 2010. p. 2642-2645.
- Vaillant, M.; Glaunes, J. Surface matching via currents, in: *Information Processing in Medical Imaging*. Springer; 2005. p. 1-5.
- Valette S, Chassery JM, Prost R. Generic remeshing of 3d triangular meshes with metric-dependent discrete voronoi diagrams. *IEEE Transactions on Visualization and Computer Graphics*. 2008; 14:369–381. [PubMed: 18192716]
- Wagner S, Auffermann W, Buser P, Semelka RC, Higgins CB. Functional description of the left ventricle in patients with volume overload, pressure overload, and myocardial disease using cine magnetic resonance imaging. *American journal of cardiac imaging*. 1991; 5:87–97. URL: <http://www.ncbi.nlm.nih.gov/pubmed/10147590>. PMID: 10147590. [PubMed: 10147590]
- Wang VY, Lam H, Ennis DB, Cowan BR, Young AA, Nash MP. Modelling passive diastolic mechanics with quantitative MRI of cardiac structure and function. *Medical Image Analysis*. 2009; 13:773–784. URL: <http://www.sciencedirect.com/science/article/pii/S1361841509000619>. [PubMed: 19664952]
- Weidemann F, Niemann M, Ertl G, Strk S. The different faces of echocardiographic left ventricular hypertrophy: clues to the etiology. *Journal of the American Society of Echocardiography: official publication of the American Society of Echocardiography*. 2010; 23:793–801. URL: <http://www.ncbi.nlm.nih.gov/pubmed/20591620>. PMID: 20591620. [PubMed: 20591620]
- Weinberg EO, Thienelt CD, Katz SE, Bartunek J, Tajima M, Rohrbach S, Douglas PS, Lorell BH. Gender differences in molecular remodeling in pressure overload hypertrophy. *Journal of the American College of Cardiology*. 1999; 34:264–273. URL: <http://www.sciencedirect.com/science/article/pii/S0735109799001655>. [PubMed: 10400020]
- Wheeler M, Pavlovic A, DeGoma E, Salisbury H, Brown C, Ashley E. A new era in clinical genetic testing for hypertrophic cardiomyopathy. *Journal of Cardiovascular Translational Research*. 2009; 2:381–391. URL: <http://www.springerlink.com/content/b1832v342x07363r/abstract/>. [PubMed: 20559996]
- Younes L. Constrained diffeomorphic shape evolution. *Foundations of Computational Mathematics*. 2012:1–31.
- Zhang X, Cowan BR, Bluemke DA, Finn JP, Fonseca CG, Kadish AH, Lee DC, Lima JAC, Suinesiaputra A, Young AA, Medrano-Gracia P. Atlas-Based Quantification of Cardiac Remodeling Due to Myocardial Infarction. *PLoS ONE*. 2014; 9:e110243. URL: <http://dx.doi.org/10.1371/journal.pone.0110243>. [PubMed: 25360520]

### Highlights

- We present advanced mathematical model to perform 3D+time cardiac shape analysis.
- We construct 3D models of left-ventricular (LV) geometry from MRI cross-sections.
- This is achieved by mapping LV triangulated surface mesh to MRI contours.
- We compared hypertrophic cardiomyopathy and hypertensive heart disease.
- Significant shape differences at ES and from ED to ES were identified.

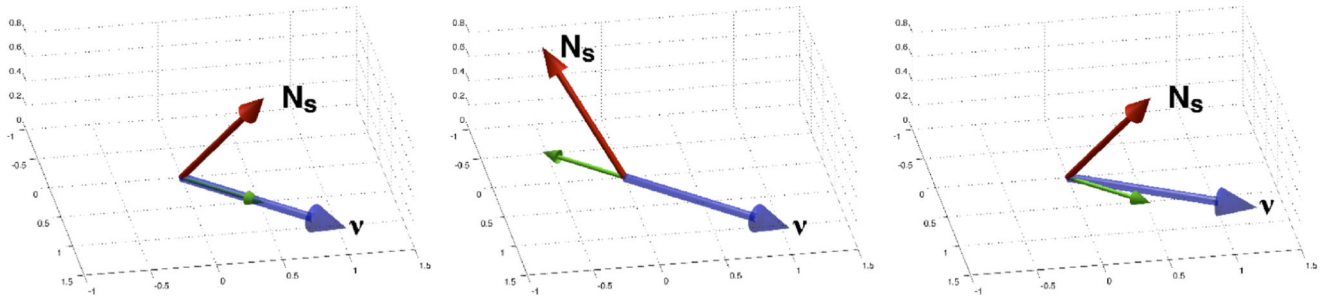


**Figure 1.** Examples of consistent (left) and non-consistent surface normal vectors (middle panel illustrates an example of antiparallel vectors and right panel illustrates an example of non-parallel vectors). Green arrow represents projection of surface normal into the horizontal plane.

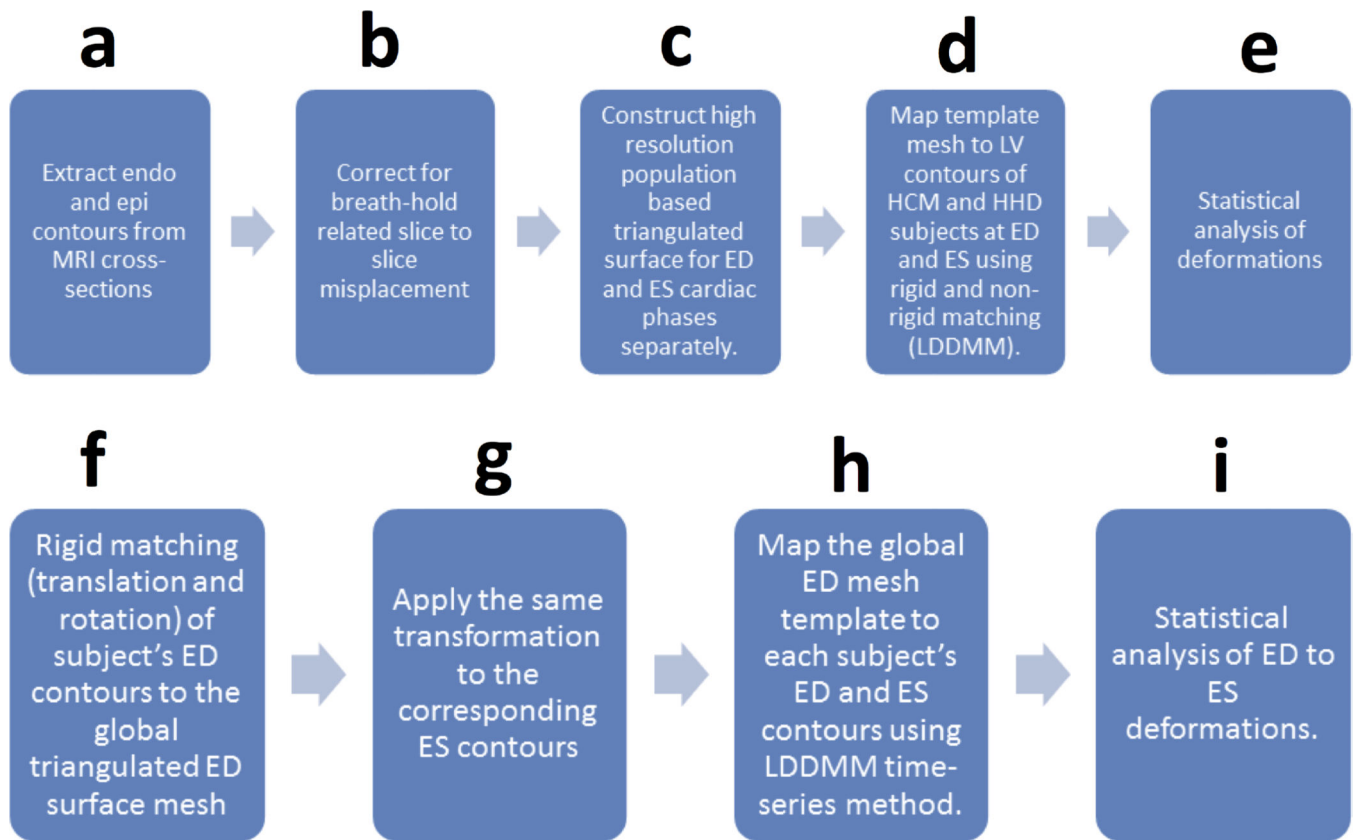


**Figure 2.** Work flow to conduct shape analysis at ED and ES cardiac phases (top panel) and from ED to ES (bottom panel).

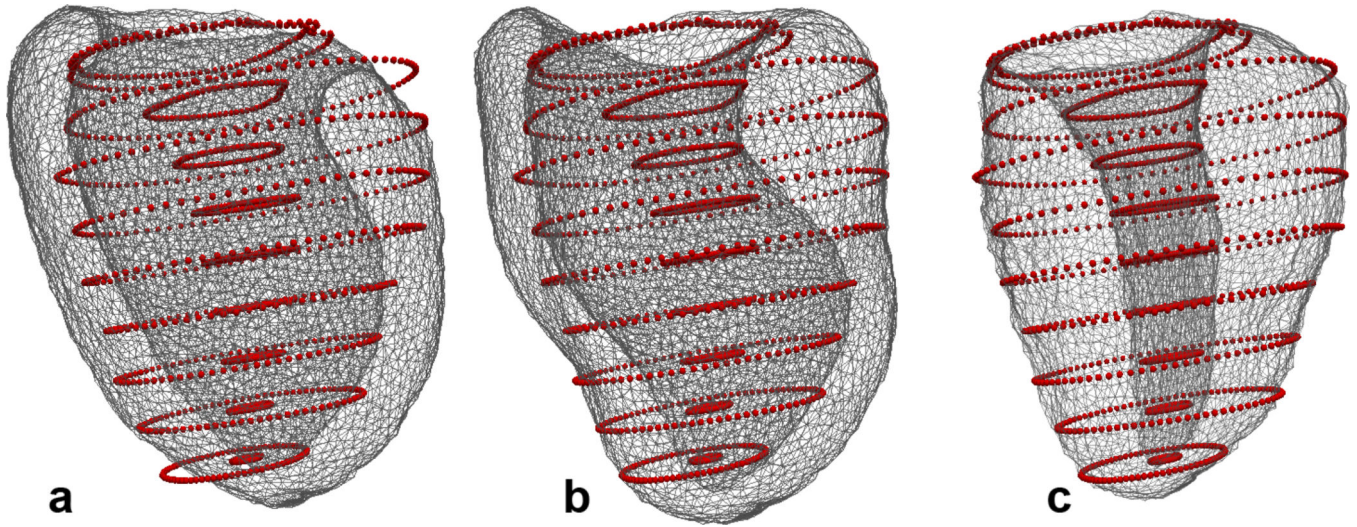


**Figure 3.**

Result of the distance matching algorithm to map a high-resolution triangulated surface (gray mesh) to sparse cross-section contours (red dots). a) Surface template and contours before matching. b) Deformed surface template and the corresponding target contours using distance matching-algorithm proposed by Ardekani et al. (Ardekani et al., 2012). c) Deformed surface template and the corresponding target contours using the distance-matching algorithm proposed in this paper. This figure provides a visual representation to highlight the importance of the method proposed in this paper. Note that defining a cost function solely based on closest points between surface nodes and contour points may attract the wrong surface to the contour due to a large variation in myocardial size (panel b).

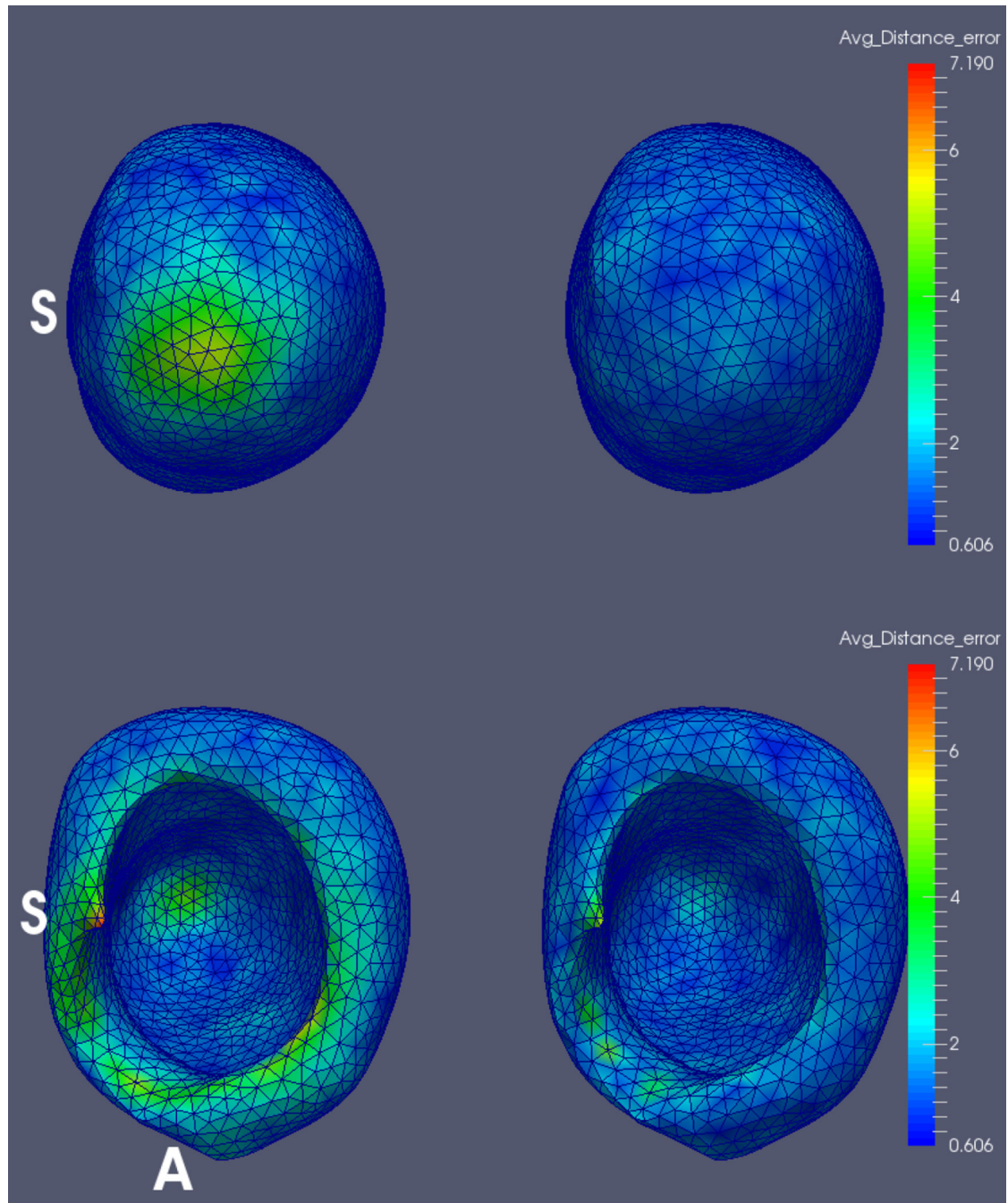


**Figure 4.** Average distance error map (mm) computed for LDDMM surface -to-curve (left column) and surface-to-surface (right column) matching. The top panel illustrates the apical view and the bottom panel illustrates the basilar view. S: septal wall, A: anterior wall

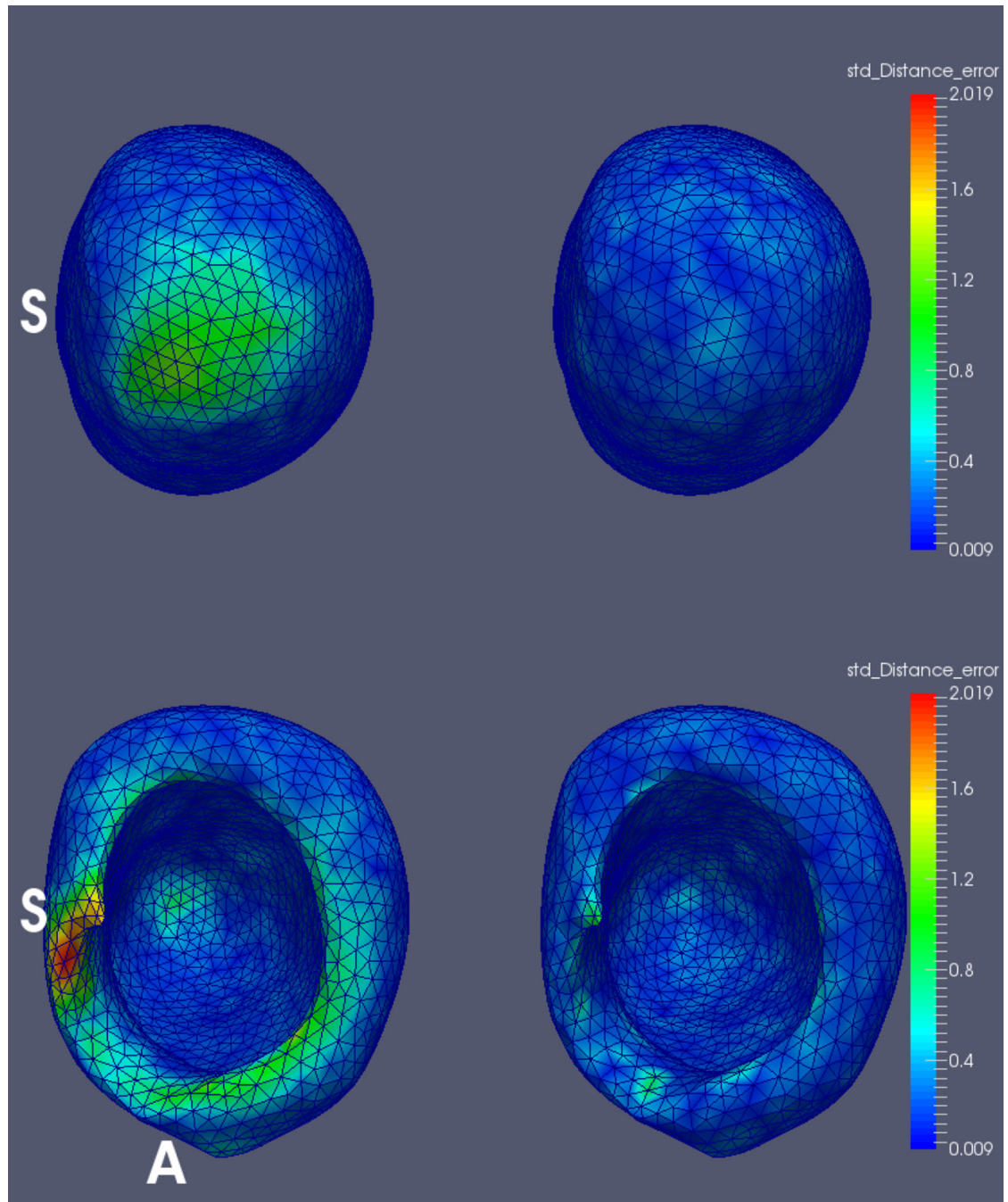


**Figure 5.** Standard deviation of distance error map (mm) computed for LDDMM surface-to-curve (left column) and surface-to-surface (right column) matching. The top panel illustrates the apical view and the bottom panel illustrates the basilar view. S: septal wall, A: anterior wall

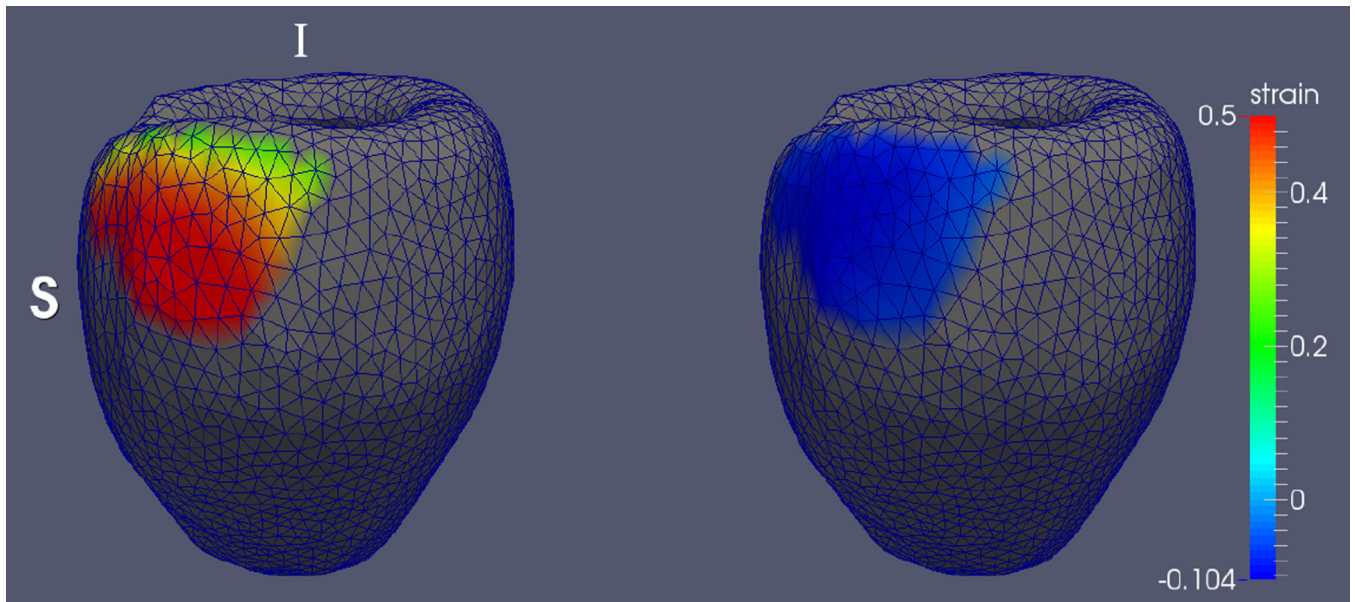


**Figure 6.** ES radial geometric strain significant map that was estimated using FWER multiple comparisons correction method was placed on the common template surface (gray mesh). Color map represents group average (per node) values of radial geometric strain for HCM (left) and HHD (right) populations at the region that was statistically significant. S: septal wall, I: inferior wall

**Table 1**

Cohort demographic and volumetric and mass measurements.

Population	n	Gender (F/M)	Mean Age	LVEF	EDLVV(mL)	ESLVV(mL)	LVM(gm)
HCM	9	5/4	45±12	67.8±7.9%	130.0±45.9	42.6±19.8	147.0±66.7
HHD	11	2/9	53±10	56.3±7.3%	168.2±61.6	76.7±39.4	136.5±42.7
Probability	-	-	0.18	0.008	0.18	0.08	0.94

LVEF: Left-ventricular ejection fraction, EDLVV and ESLVV: Left-ventricular volumes at ED and ES respectively, LVM: LV mass. P-values are based on ranksum test.

**Table 2**

Pattern of hypertrophy in HCM patients.

Subjects	Basilar	Mid	Apical
1	Ant. wall,Septum	Septal	Septal
2	Ant.,Sept.,Inf.	Ant.,Sept.,Inf.	Ant.,Sept.,Inf.
3	Ant. wall	Inf. wall	Inf. wall
4		Septum, Lat.,Inf. wall	Septum, Lat.,Inf. wall
5	Sept.,Ant.	Ant.,Sept.,Inf.	Ant.,Sept.,Inf.,Lat.
6	Ant. wall,septum		
7	Septum, Ant.,Inf. wall	Septum, Ant.,Inf. wall	
8	Septum, Ant. wall	Septum, Ant. wall	Inf. wall
9	Ant. wall	Ant. wall	

Ant.: anterior, Sept.: septum, Inf.: inferior

Average closest point distance error in mm after (before) template estimation among 5 different templates (hypertemplates).

**Table 3**

Template No.	1	2	3	4	5
1	0	1.55 (2.58)	1.56 (2.61)	1.65 (4.87)	1.57 (2.69)
2	1.57 (2.88)	0	1.59 (2.9)	1.7 (4.64)	1.59 (3.24)
3	1.59 (3.11)	1.6 (3.06)	0	1.66 (5.77)	1.56 (2.65)
4	1.69 (4.64)	1.68 (4.19)	1.65 (5.17)	0	1.67 (4.41)
5	1.61 (3.00)	1.6 (3.13)	1.57 (2.41)	1.71 (4.91)	0